

Herpers, A., O'Shea, K. J., MacLaren, D. A., Noyong, M., Rösger, B., Simon, U., and Dittmann, R. (2014) *Competing strain relaxation mechanisms in epitaxially grown $Pr_{0.48}Ca_{0.52}MnO_3$ on $SrTiO_3$* . APL Materials, 2 (10). p. 106106. ISSN 2166-532X

Copyright © 2014 The Authors

<http://eprints.gla.ac.uk/98979/>

Deposited on: 04 November 2014

Competing strain relaxation mechanisms in epitaxially grown $\text{Pr}_{0.48}\text{Ca}_{0.52}\text{MnO}_3$ on SrTiO_3

Anja Herpers, Kerry J. O'Shea, Donald A. MacLaren, Michael Noyong, Bernd Rösger, Ulrich Simon, and Regina Dittmann

Citation: *APL Materials* **2**, 106106 (2014); doi: 10.1063/1.4900817

View online: <http://dx.doi.org/10.1063/1.4900817>

View Table of Contents: <http://scitation.aip.org/content/aip/journal/aplmater/2/10?ver=pdfcov>

Published by the AIP Publishing

Articles you may be interested in

Coupling of magnetic field and lattice strain and its impact on electronic phase separation in $\text{La}_{0.335}\text{Pr}_{0.335}\text{Ca}_{0.33}\text{MnO}_3$ /ferroelectric crystal heterostructures
Appl. Phys. Lett. **103**, 263507 (2013); 10.1063/1.4860415

The effects of strain, current, and magnetic field on superconductivity in $\text{Pr}_{0.5}\text{Ca}_{0.5}\text{MnO}_3/\text{YBa}_2\text{Cu}_3\text{O}_7/\text{Pr}_{0.5}\text{Ca}_{0.5}\text{MnO}_3$ trilayer
J. Appl. Phys. **113**, 113902 (2013); 10.1063/1.4795349

Strain effect caused by substrates on phase separation and transport properties in $\text{Pr}_{0.7}(\text{Ca}_{0.8}\text{Sr}_{0.2})_{0.3}\text{MnO}_3$ thin films
J. Appl. Phys. **111**, 07D721 (2012); 10.1063/1.3678297

Misfit strain dependence of ferroelectric and piezoelectric properties of clamped (001) epitaxial $\text{Pb}(\text{Zr}_{0.52}\text{Ti}_{0.48})\text{O}_3$ thin films
Appl. Phys. Lett. **99**, 252904 (2011); 10.1063/1.3669527

Epitaxial $\text{Sr}_{1.8}\text{Ca}_{0.2}\text{NaNb}_5\text{O}_{15}$ thin film waveguides grown by pulsed laser deposition: Optical properties and microstructure
J. Appl. Phys. **106**, 073523 (2009); 10.1063/1.3239991



Goodfellow

metals • ceramics • polymers
composites • compounds • glasses

Save 5% • Buy online
70,000 products • Fast shipping

www.goodfellowusa.com

Competing strain relaxation mechanisms in epitaxially grown $\text{Pr}_{0.48}\text{Ca}_{0.52}\text{MnO}_3$ on SrTiO_3

Anja Herpers,¹ Kerry J. O'Shea,² Donald A. MacLaren,² Michael Noyong,³ Bernd Rösger,¹ Ulrich Simon,³ and Regina Dittmann¹

¹Research Center Jülich, Peter Grünberg Institut, Electronic Materials (PGI-7), 52425 Jülich, Germany

²SUPA, School of Physics and Astronomy, University of Glasgow, Glasgow G12 8QQ, United Kingdom

³Institute of Inorganic Chemistry (IAC), RWTH Aachen University, Landoltweg 1, 52074 Aachen, Germany

(Received 28 August 2014; accepted 20 October 2014; published online 31 October 2014)

We investigated the impact of strain relaxation on the current transport of $\text{Pr}_{0.48}\text{Ca}_{0.52}\text{MnO}_3$ (PCMO) thin films grown epitaxially on SrTiO_3 single crystals by pulsed laser deposition. The incorporation of misfit dislocations and the formation of cracks are identified as competing mechanisms for the relaxation of the biaxial tensile strain. Crack formation leads to a higher crystal quality within the domains but the cracks disable the macroscopic charge transport through the PCMO layer. Progressive strain relaxation by the incorporation of misfit dislocations, on the other hand, results in a significant decrease of the activation energy for polaron hopping with increasing film thickness. © 2014 Author(s). All article content, except where otherwise noted, is licensed under a Creative Commons Attribution 3.0 Unported License. [<http://dx.doi.org/10.1063/1.4900817>]

Mixed-valence manganites form a class of perovskite oxides that excel in their large diversity of electrical properties and their complexity of magnetic phase diagrams. The transport and magneto transport properties depend strongly on the specific cation species, their stoichiometry and the resulting structural properties.^{1,2} As a result of their manifold functional properties, these materials offer a broad variety of applications as thin films in sensors, magnetic and magneto-resistive devices, redox-based data storage, and fuel cells.³ In addition, they show valuable properties as high-temperature superconductivity or giant elastoresistance.^{4–8} $\text{Pr}_{1-x}\text{Ca}_x\text{MnO}_3$, in particular, has been successfully used in resistive switching devices, which are based on redox-process driven metal-to-insulator transitions.^{9–14}

For epitaxially grown manganite thin films, the combination of strain state and defect structure can influence both the electrical and magnetic properties of the system, as the electronic structure of these strongly correlated systems depends sensitively on the lattice parameters and the bond angles. The transport mechanism of mixed valence manganites depends strongly on the choice of A-site cations and the doping level but also on the temperature range and oxygen environment. For highly doped $\text{Pr}_{1-x}\text{Ca}_x\text{MnO}_3$, the charge transport is known to be polaron hopping: Specifically, the hopping of holes that are trapped in their own Jahn-Teller lattice distortion. Due to the extremely high doping level, the system can be described as a degenerate p-type semiconductor.^{15,16}

Grown on the commonly used substrate material SrTiO_3 (STO), $\text{Pr}_{1-x}\text{Ca}_x\text{MnO}_3$ has to face a mismatch strain, $\varepsilon_m = (a_f - a_s)/a_s$, ranging between -4.70% for CaMnO_3 ($x = 1$) and $+0.26\%$ for PrMnO_3 ($x = 0$), where a_f and a_s are the (pseudo)-cubic lattice constants of film and substrate, respectively.¹⁷ This results in tensile strain for the vast majority of stoichiometries.¹⁸ In particular, the composition $\text{Pr}_{0.48}\text{Ca}_{0.52}\text{MnO}_3$ (PCMO) used in this paper has a lattice mismatch of -2.39% .

For epitaxially grown thin films under mild tensile strain, the most common relaxation mechanism is the incorporation of misfit dislocations.¹⁹ Depending on the brittleness of the material, the formation of cracks has been observed as an alternative strain relaxation mechanism.^{20–22} Additionally, interfacial reconstruction and oxygen vacancy ordering are also reported as strain relaxation mechanisms in complex oxides.^{23,24}

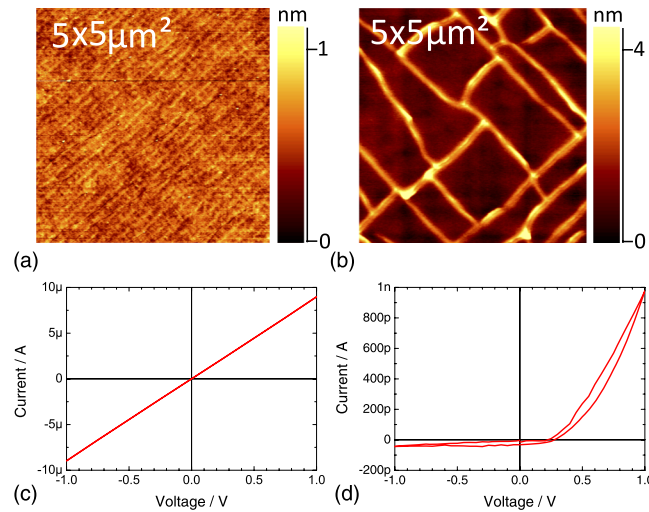


FIG. 1. AFM images and corresponding I - V characteristics of two 50 nm thick PCMO films grown on STO and found to have different structural and electrical properties. The I - V characteristics are in-plane measurements through PCMO on STO using Pt contacts: (a) AFM image of an atomically flat film with $R_q = 1.3$ Å. The image edges are aligned along STO (100) and (010) directions. (b) Topography of a PCMO film with line-pattern on top, $R_q = 9.2$ Å, aligned along STO (110) and (110). (c) Typical ohmic behavior from a sample similar to that of (a), with a resistance of approximately 100 kΩ. (d) Rectifying I - V measurement with low currents, from a sample similar to that of (b).

In this work, we investigated in detail the impact of strain relaxation mechanisms on electric current transport in PCMO thin films that were grown epitaxially by pulsed laser deposition (PLD) on STO substrates. The progressive strain relaxation with increasing film thickness was studied by atomic force microscopy (AFM), X-ray diffraction (XRD) and scanning transmission electron microscopy (STEM). We find that both mechanisms for strain relaxation—i.e., plastic stress deformation as well as crack formation—occur and differ crucially in their impact on the structural and electrical properties of the thin films.

PCMO thin films were grown epitaxially on (001)-oriented STO substrates by PLD. To ensure an atomically flat step terrace surface structure, the substrates were annealed for four hours in air at 950 °C prior to deposition, which was then performed using 0.133 mbar O₂ ambient pressure, 700 °C substrate temperature, 5 Hz pulse frequency, and 2.8 J/cm² laser fluence ($\lambda = 248$ nm). After the deposition, the samples were immediately cooled down in an O₂ pressure of 500 mbar.

50 nm thick PCMO films were found to exhibit two distinctly different surface structures. Some films were smooth, with a regular step terrace structure that derives from the underlying substrate's miscut, as shown in the AFM image in Figure 1(a), which has a roughness of $R_q = 1.3$ Å and is dominated by steps of height 3.8 Å, corresponding to the pseudo-cubic unit cell dimension of PCMO.¹⁸ However, the surface structures of a large number of samples are dominated by a regular pattern of orthogonal lines that typically align along the STO (100) and (010) crystal axes. These features are 2–3 nm high and punctuate the otherwise smooth surface, as illustrated by the sample of Figure 1(b), which has an increased roughness of $R_q = 9.2$ Å. The lines are separated by distances ranging from several 100 nm to several micrometers, which for some samples crucially depends on the crystal direction. The regions between the line features retain a stepped morphology, similar to that of Figure 1(a). These morphological film-to-film variations could not be correlated to any systematic changes in the deposition conditions. There was also no obvious correlation of the lines or their periodicity to the underlying STO miscut angle, which has been shown to be important in other material systems.^{25,26} Variations in surface preparation of the STO substrate by changing the annealing time or applying an additional etching step to terminate the surface by TiO₂ did not affect the type of relaxation as well. However, the substrate orientation has not been changed, and, especially, there was no feasibility to investigate the influence of variations of the dislocation density in the STO substrates on the strain relaxation, which could have a crucial impact.

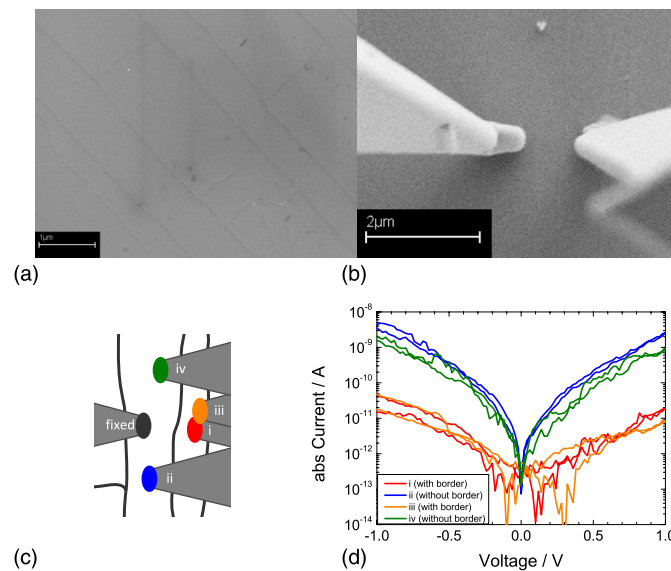


FIG. 2. SEM-assisted micro-probe conductance measurements: (a) SEM image of the surface of 50 nm PCMO on STO, showing the line pattern. (b) An example SEM image showing the positioning of the AFM tips for conductance measurements, in this case for measurement i, which straddles a line in the surface. (c) Schematic image of the four measured tip positions, i–iv, relative to the line pattern. (d) I - V characteristics of the four different in-plane measurements according to the geometries in (c).

For the electrical characterization of the PCMO thin films, 50 nm thick platinum top electrodes with a diameter of 70 μm were sputter-deposited through a shadow mask and electrically accessed by tungsten needles. The high work function metal Pt²⁷ is a suitable choice because it forms an ohmic contact at the interface to p-type PCMO,^{9,12} so that contact resistances can be neglected. For most lateral two-point measurements over distances in the millimeter-range, the expected linear characteristic with an ohmic resistance in the order of 100 kΩ was observed, as shown in Figure 1(c). However, for several samples, I - V curves with rectifying behavior and very low currents below 1 nA were also measured, as depicted in Figure 1(d). All samples exhibiting a rectifying I - V measurement were proven to show the line pattern.

In order to clarify if the non-ohmic I - V characteristics relate to the observed line pattern shown in Figure 1(b), the microscopic transport properties of such a line-patterned PCMO thin film were investigated. A nanorobotic station²⁸ was used to measure the transport within a single domain of the PCMO film and across such a line. The four nanomanipulators are equipped with Pt/Ir metallized AFM tips. The tip positioning is assisted by scanning electron microscopy (SEM), which enables the precise arrangement of the AFM tips with respect to the line pattern of the PCMO surface, as illustrated in Figure 2(a). Electrical measurements were performed for the four different tip positions (named i–iv), illustrated in Figure 2(b) for measurement i. The line pattern is hardly visible in the SEM image containing the two AFM tips but the tip positions relative to the line pattern on the PCMO surface are sketched in Figure 2(c). The left tip was fixed in position while the right tip was repositioned between measurements, alternating the tip position from neighboring domain (measurements i and iii) to measurements of the same domain as the left tip (measurements ii and iv). The resulting I - V -curves are depicted in Figure 2(d) and show clear anisotropy. It is interesting to note that a difference of two orders of magnitude in current is reproducibly observed between measurements within a single domain and across a line. Consequently, the blocking property of the individual lines can explain the macroscopic non-ohmic I - V characteristics of the line-pattern samples.

To elucidate the microstructure beneath the lines seen by SEM and AFM, the PCMO sample was investigated by cross-sectional STEM. An electron-transparent lamella was prepared by focused ion beam (FIB) sectioning from the sample stack, using an FEI Nova Dualbeam FIB-SEM that was also equipped with a gas injection source for the deposition of a protective Pt capping layer

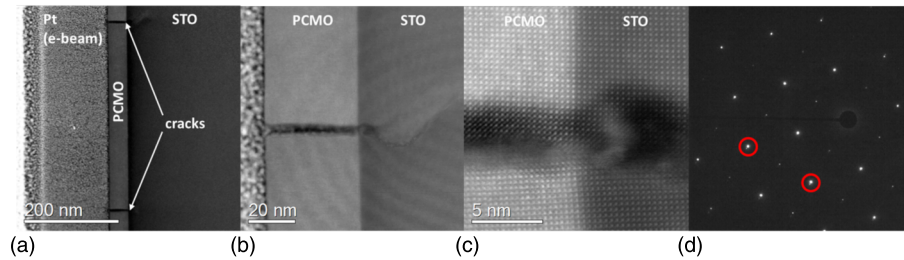


FIG. 3. Cross-sectional STEM images of a 40 nm PCMO/STO sample showing the line pattern. The cross-section was formed after deposition of a protective Pt capping layer: (a) $500 \times 500 \text{ nm}^2$ HAADF image, (b) $100 \times 100 \text{ nm}^2$ close-up view of one crack, (c) $15 \times 15 \text{ nm}^2$ close-up of the interface region near the crack, (d) diffraction pattern highlighting spot splitting resulting from the crack (red circles).

prior to FIB milling. STEM was conducted on a JEOL ARM cFEG instrument operated at 200 kV, typical dark field images and a selected area diffraction pattern are presented in Figure 3.

The STEM images of the line-pattern sample in Figure 3 clearly identify the elevated lines as ridges at the edges of deep cracks that lie perpendicular to the interface and which propagate through the entire PCMO film. It is also worth noting that the cracks extend through the PCMO thin film into the STO substrate itself, which suggests that they form post-deposition, presumably in response to substantial strain. A tension field becomes visible (Figure 3(b)) in the PCMO film and STO substrate through the curved, weak Moiré fringes that arise from a mismatch between the periodicity of the STEM scanning raster pattern and the crystallographic periodicity.^{29,30} Both the low magnification image in Figure 3(b) and the atom-resolved image of Figure 3(c) indicate otherwise good epitaxial growth of the PCMO onto the STO. The crack tilts slightly the different domains away from each other, thereby releasing the tensile strain and allowing the PCMO layer to relax (Figure 3(c)). The strain field is also visible in the selected area diffraction pattern in Figure 3(d), which shows a spot splitting, one set of spots for each side of the crack. For these types of samples, the substrate-induced biaxial strain is clearly released by the formation of cracks that can explain both the microscopic and macroscopic transport properties of the line-patterned PCMO thin films. Since the cracks extend throughout the PCMO film, domains separated by a crack are very poorly connected electrically.

In contrast to the cracked sample of Figure 3, Figure 4 summarizes a STEM analysis of the smooth, crack-free sample that is shown in Figure 1(a). Low magnification images (not shown) indicated the PCMO film to be smooth, continuous, and crack-free. The individual columns of cations are clearly resolved in the high magnification high-angle annular dark field (HAADF) image of Figure 4(a), and the epitaxial relationship between film and substrate is again clear. However, dislocations are readily identified by Fourier filtering (Figures 4(b) and 4(c)). The filtered image in Figure 4(d) derives from only those spots encircled in the Fourier transform in Figure 4(b) and selects (001)-type fringes (perpendicular to the surface). It reveals a (001)-type edge dislocation within the PCMO layer, around 1.5 nm above the STO interface. In a larger STEM section of

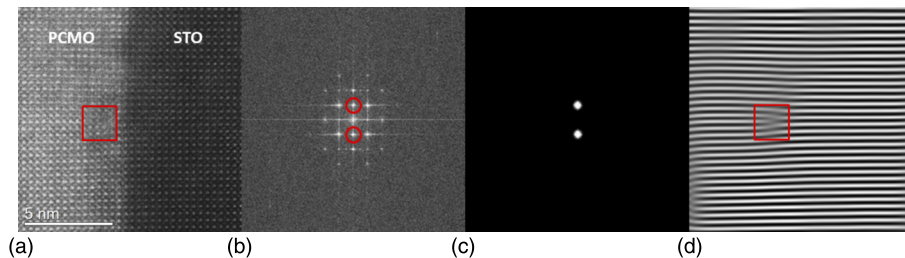


FIG. 4. Cross-sectional STEM images of a 50 nm PCMO/STO sample with a smooth surface: (a) $20 \times 20 \text{ nm}^2$ HAADF image, (b) Fourier transform of (a), (c) Fourier transform after masking relevant frequencies, (d) inverse Fourier transform of masked image.

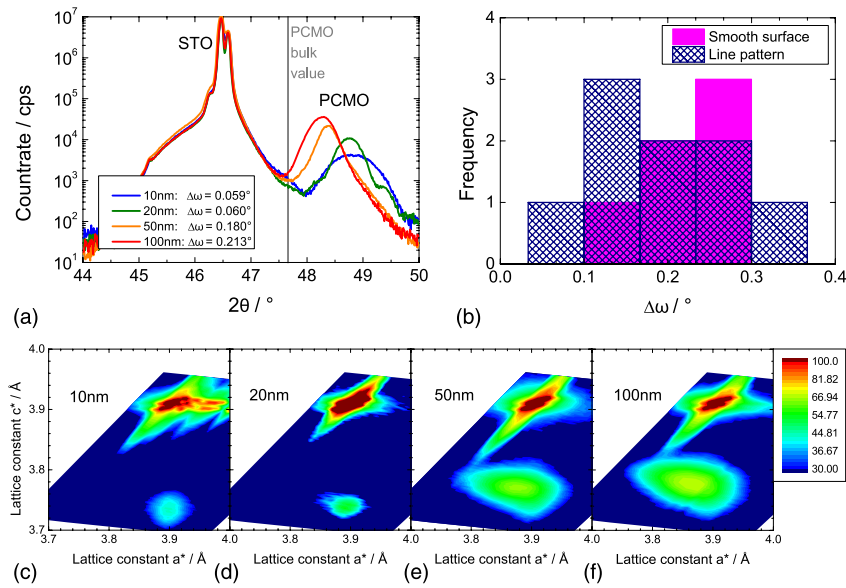


FIG. 5. Thickness dependence of the structural properties of epitaxial PCMO thin films on STO: (a) XRD diffractograms around the STO (002) reflex from samples with a PCMO thickness of 10 nm, 20 nm, 50 nm, and 100 nm, respectively. (b) Frequency distribution of the rocking curve widths (full width half maximum values, $\Delta\omega$) for both types of 50 nm thick PCMO samples from Figure 1. (c)–(f) RSMs around STO (103), corresponding to the samples in Figure 5(a).

$50 \times 50 \text{ nm}^2$ (not shown), two such dislocations can be identified. We, therefore, conclude that for this type of PCMO thin film, the stress is relaxed by the formation of misfit dislocations.

To investigate further the relaxation behavior of these crack-free films, the PCMO film thickness was varied in four steps, from 10 nm to 100 nm. All four thin films exhibited an atomically flat surface with a roughness of $R_q = 2.1\text{--}2.6 \text{ \AA}$. XRD was used to determine the out-of-plane lattice constants by measuring the diffractograms around the STO (002) Bragg reflex, as depicted in Figure 5(a). With increasing film thickness, the lattice c^* -axis is enlarged towards the bulk value for PCMO, $a_b^* = 3.814 \text{ \AA}$.

The evolution of the in-plane lattice constant was obtained by measuring reciprocal space maps (RSM) around the STO (103) Bragg reflection. These maps are plotted in Figures 5(c)–5(f) for PCMO film thicknesses of 10 nm, 20 nm, 50 nm, and 100 nm. For the 10 nm and 20 nm thick samples, the a^* -axes of film and substrate match perfectly, while the c^* -axis is reduced compared to the bulk value. Above a thickness of 20 nm, both the a^* - and c^* -axes of the PCMO film relax towards their bulk values but do not achieve them. This observation is in broad agreement with STEM data (not shown) that show a similar increase in c^* with increasing distance from the interface.

The density of dislocations necessary to relax the system completely can be calculated from geometrical considerations according to the Matthews-Blakeslee model.^{19,31,32} For the assumption of a very thick PCMO film with $d \gg d_c$, which is valid in this case, this dislocation density is given by $\xi_d = (a_s - a_f^*) / (a_s \cdot a_f^*)$. For the PCMO thin film on STO, a value of $\xi_d \approx 6 \times 10^{-2} \text{ nm}^{-1}$ is obtained, leading to three dislocations within an average 50 nm. As the XRD data suggest that the 50 nm thick PCMO film is not completely relaxed (Figure 5(e)), leading to a reduced number of expected misfit dislocations, this value agrees well with the separation of the two dislocations observed by STEM.

The critical thickness for the formation of misfit dislocations d_c can also be estimated^{31,32} and is calculated to be 1.4 nm (using Poisson's ratio of $\nu = 1/3$ and a cutoff parameter of $\alpha = 4$), in good agreement with the location of the dislocation found in Figure 4. This stand-off distance was also observed for $\text{Ba}_{1-x}\text{Sr}_x\text{TiO}_3$ grown on STO.³³

However, the results from the thickness series of PCMO (Figure 5) show that the relaxation process starts at a thickness between 20 nm and 50 nm. A possible explanation for this discrepancy is that the Matthews-Blakeslee approach neglects a number of factors that are significant for complex oxides

and which increase the energy for nucleation and motion of dislocations in these systems. These factors include the periodic step-terrace interface structure, electrostatic repulsion and forces between second-nearest neighbors of equal charge.³² Kinetic limitations during PCMO thin film growth might additionally lead to deviations from the homogeneous equilibrium distribution of dislocations.³⁴

Another explanation for the discrepancy between the Matthews-Blakeslee approach and experiment may be that alternative mechanisms for strain relaxation³⁵ occur for film thicknesses between 1.5 nm and 20 nm. For mixed-valence manganites, for instance, these could be bond angle adjustments,³⁶ octahedral tilts,³⁷ oxygen vacancy ordering,²⁴ or spin-state ordering.³⁸

Figure 5(a) shows that the rocking curve width increases with increasing film thickness up to a factor of 3. This is a result of the incorporation of edge dislocations. In the proximity of the dislocation core, a mosaic structure is induced.⁴ Different degrees of the tilting of the out-of-plane axis lead to a broadening of the rocking curves of the PCMO Bragg reflexes with increasing degree of strain relaxation. However, the effect is absent for the cracked PCMO films, as confirmed by a comparison of the rocking curve widths of the two types of PCMO thin films in Figure 5(b). The rocking curves for 50 nm thick smooth and cracked PCMO samples were determined and their distributions are depicted. Despite the poor statistics, a clear difference between the centers of both distributions is discernible and shows a sharper rocking curve for cracked PCMO films, but a broader distribution for smooth films. We additionally analyzed 50 nm PCMO thin films deposited epitaxially on 30 nm SrRuO₃ on STO, which showed a similar statistics.

Summarizing the structural data, we have observed that strain relaxation in PCMO thin films grown on STO substrates occurs by either the formation of misfit dislocations or by the formation of cracks, depending on the details of growth. In one case, epitaxial strain is relieved through incorporation of regular dislocation defects, in the other case, it may be that density of dislocations is lower and that strain relief is less complete, leading to a more catastrophic relief through the formation of cracks. Although the formation energy of misfit dislocations is expected to be lower than the energy required for crack formation, the formation of a sufficient density of strain-relieving dislocations during growth may be inhibited by kinetic limitations. Dislocations are required to occur regularly and with a density that is sufficient to relax the system. However, if the available thermal energy and time are not sufficient for the dislocations to evolve and move to form a regular lattice during growth, then the additional strain may cause cracking while the sample is cooling after growth. Even though all investigated thin films were grown under nearly the same deposition conditions, there could be slight differences in the defect structure within the films or the substrates, which could modify the nucleation and movement of dislocations during growth. Furthermore, the details of the cooling procedure could influence the strain relaxation crucially, since plastic relaxation by dislocation formation might be possible in the early stages of cooling, whereas it will be inhibited at a later stage. On the other hand, crack formation might occur in the final stage of cooling or even at room temperature, if the PCMO thin films have been insufficiently relaxed by the formation of dislocations at high temperatures.

To summarize the above results, our microstructural and electrical analyses clearly show that PCMO thin films with microcracks are not suitable to investigate the correlation between strain state and charge transport. We, therefore, performed temperature dependent resistivity measurements on different film thicknesses in a van-der-Pauw geometry³⁹ using only crack-free PCMO samples. Figure 6 reveals the temperature and thickness dependence of the electrical resistivity, ρ , of the PCMO thin films. The resistivity of all three samples can be fitted using small polaron hopping as the active transport mechanism according to

$$I(T) = \frac{ne\omega A}{\pi} \cdot e^{-\frac{\Delta E}{k_B T}} \cdot \sinh\left(\frac{ea}{2k_B T r} \cdot V\right) \approx \frac{ne^2 a^2 \omega A V}{2\pi k_B T r} \cdot e^{-\frac{\Delta E}{k_B T}} \Leftrightarrow \rho(T) \approx \frac{2\pi k_B T}{ne^2 a^2 \omega} \cdot e^{\frac{\Delta E}{k_B T}}, \quad (1)$$

in the adiabatic limit,^{11,40} where n is the polaron density, e is the electronic charge, a is the hopping distance, ω is the phonon frequency, ΔE is the activation energy, k_B is the Boltzmann constant, T is the temperature, and A and r denote the area and thickness of the film, respectively.

The activation energy for polaron transport, ΔE , is reduced by 10% with increasing film thickness. This increase in polaron binding energy, $2\Delta E$, with decreasing film thickness has been reported in literature⁴¹ for superlattices consisting of La_{1-x}Ca_xMnO₃/SrTiO₃ and La_{1-x}Ca_xMnO₃/NdGaO₃.

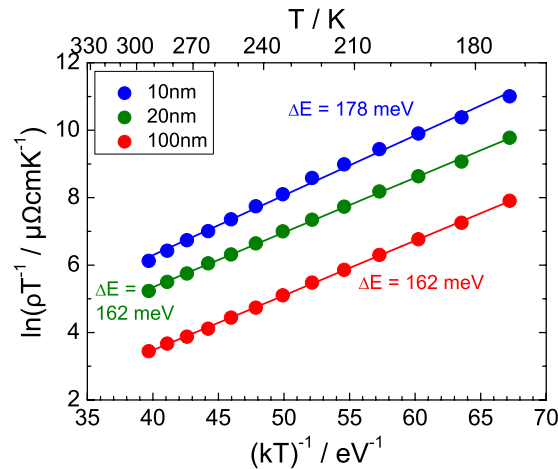


FIG. 6. Thickness dependence of the electrical properties of crack-free epitaxial PCMO thin films on STO. Temperature dependence of the resistivity for PCMO films with thickness 10 nm, 20 nm, and 100 nm (Figure 5).

They attributed it to an enhancement of the Jahn-Teller distortion with increasing tensile strain in the ultrathin films, which should increase the polaron binding energy. Furthermore, the intercept of the linear fit changes for the different film thicknesses, which can, however, not be explained with the same underlying mechanisms.

In conclusion, we have shown that tensile strain in PCMO thin films can be relaxed by two different mechanisms. Crack formation leads to a higher crystal quality within the domains but the cracks disable the macroscopic charge transport through the PCMO layer. Progressive strain relaxation by the incorporation of misfit dislocations, on the other hand, allows the investigation of strain-dependent charge transport. The charge transport through the PCMO film by field induced polaron hopping is conserved upon relaxation, but the changes in lattice constants directly affect the Jahn-Teller distortions, which influence the barrier for polaron hopping and, thus, the resistivity of PCMO.

This work was funded by the European Union Council under the 7th Framework Program (FP7) Grant No. 246102 IFOX and has been in part supported by the Deutsche Forschungsgemeinschaft (SFB 917). We furthermore acknowledge additional funding from the W2/W3 program of the Helmholtz association. DAM is grateful for a fellowship from the Engineering and Physical Sciences Research Council of the UK (EP/I00419X/1).

- ¹ L. P. Gor'kov and V. Z. Kresin, *Phys. Rep.* **400**, 149 (2004).
- ² J. M. D. Coey, M. Viret, and S. von Molnar, *Adv. Phys.* **48**, 167 (1999).
- ³ P. Shuk, A. Vechev, V. Kharton, L. Tichonova, H. Wiemhofer, U. Guth, and W. Gopel, *Sens. Actuators, B* **15-16**, 401 (1993).
- ⁴ S. C. Wimbush, M. Li, M. E. Vickers, B. Maiorov, D. M. Feldmann, Q. Jia, and J. L. MacManus-Driscoll, *Adv. Funct. Mater.* **19**, 835 (2009).
- ⁵ A. D. Rata, A. Herklotz, K. Nenkov, L. Schultz, and K. Doerr, *Phys. Rev. Lett.* **100**, 76401 (2008).
- ⁶ A. Asanuma, Y. Tomioka, H. Kuwahara, and Y. Tokura, *Nature* **388**, 50 (1997).
- ⁷ S. P. Jiang, *J. Mater. Sci.* **43**, 6799 (2008).
- ⁸ A. Sawa, *Mater. Today* **11**, 28 (2008).
- ⁹ K. Tsubouchi, I. Ohkubo, H. Kumigashira, M. Oshima, Y. Matsumoto, K. Itaka, T. Ohnishi, M. Lippmaa, and H. Koinuma, *Adv. Mater.* **19**, 1711 (2007).
- ¹⁰ C. Jooss, L. Wu, T. Beetz, R. F. Klie, M. Beleggia, M. A. Schofield, S. Schramm, J. Hoffmann, and Y. Zhu, *Proc. Natl. Acad. Sci. U. S. A.* **104**, 13597 (2007).
- ¹¹ S. Schramm, J. Hoffmann, and C. Jooss, *J. Phys.: Condens. Matter* **20**, 395231 (2008).
- ¹² S. Asanuma, H. Akoh, H. Yamada, and A. Sawa, *Phys. Rev. B* **80**, 235113 (2009).
- ¹³ F. Borgatti, C. Park, A. Herpers, F. Offi, R. Egoavil, Y. Yamashita, A. Yang, M. Kobata, K. Kobayashi, J. Verbeeck, G. Panaccione, and R. Dittmann, *Nanoscale* **5**, 3954 (2013).
- ¹⁴ A. Herpers, C. Lenser, C. Park, F. Offi, F. Borgatti, G. Panaccione, S. Menzel, R. Waser, and R. Dittmann, *Adv. Mater.* **26**, 2730 (2014).
- ¹⁵ D. Reagor, S. Lee, Y. Li, and Q. Jia, *J. Appl. Phys.* **95**, 7971 (2004).
- ¹⁶ A. Sawa, T. Fujii, M. Kawasaki, and Y. Tokura, *Appl. Phys. Lett.* **86**, 112508 (2005).
- ¹⁷ L. Ben Freund and S. Suresh, *Thin Film Materials, Stress, Defect Formation and Surface Evolution* (Cambridge University Press, 2013).

- ¹⁸ Database ICSD, 2014 available at: <http://www.fiz-karlsruhe.de/icsd.html>.
- ¹⁹ J. W. Matthews and A. E. Blakeslee, *J. Cryst. Growth* **27**, 118 (1974).
- ²⁰ H. Peng, B. Zhao, Z. Xie, Y. Lin, B. Zhu, Z. Hao, H. Tao, B. Xu, C. Wang, H. Chen, and F. Wu, *Phys. Rev. Lett.* **82**, 362 (1999).
- ²¹ M. Fujimoto, H. Koyama, Y. Nishi, T. Suzuki, S. Kobayashi, Y. Tamai, and N. Awaya, *J. Am. Ceram. Soc.* **90**, 2205 (2007).
- ²² Y. Wang, S. G. Kim, and I. W. Chen, *Acta Mater.* **56**, 5312 (2008).
- ²³ Y. Zhu, A. Chen, H. Zhou, W. Zhang, J. Narayan, J. L. MacManus-Driscoll, Q. Jia, and H. Wang, *APL Mater.* **1**, 50702 (2013).
- ²⁴ J. Gazquez, S. Bose, M. Sharma, M. A. Torija, S. J. Pennycook, C. Leighton, and M. Varela, *APL Mater.* **1**, 012105 (2013).
- ²⁵ Y. B. Chen, M. B. Katz, X. Q. Pan, C. M. Folkman, R. R. Das, and C. B. Eom, *Appl. Phys. Lett.* **91**, 031902 (2007).
- ²⁶ C. Ma, M. Liu, G. Collins, H. Wang, S. Bao, X. Xu, E. Enriquez, C. Chen, Y. Lin, and M. Whangbo, *ACS Appl. Mater. Interfaces* **5**, 451 (2013).
- ²⁷ H. B. Michaelson, *J. Appl. Phys.* **48**, 4729 (1977).
- ²⁸ M. Noyong, K. Blech, A. Rosenberger, V. Klocke, and U. Simon, *Meas. Sci. Technol.* **18**, N84 (2007).
- ²⁹ D. Su and Y. Zhu, *Ultramicroscopy* **110**, 229 (2010).
- ³⁰ S. Kim, S. Lee, Y. Oshima, Y. Kondo, E. Okunishi, N. Endo, J. Jung, G. Byun, S. Lee, and K. Lee, *Appl. Phys. Lett.* **102**, 161604 (2013).
- ³¹ J. S. Speck and W. Pompe, *J. Appl. Phys.* **76**, 466 (1994).
- ³² E. Breckenfeld, A. B. Shah, and L. W. Martin, *J. Mater. Chem. C* **1**, 8052 (2013).
- ³³ J. Q. He, E. Vasco, C. L. Jia, R. Dittmann, and R. H. Wang, *J. Appl. Phys.* **97**, 104907 (2005).
- ³⁴ H. Jia-Qing, E. Vasco, R. Dittmann, and W. Ren-Hui, *Chin. Phys. Lett.* **23**, 1269 (2006).
- ³⁵ S. J. Pennycook, H. Zhou, M. F. Chisholm, A. Y. Borisevich, M. Varela, J. Gazquez, T. J. Pennycook, and J. Narayan, *Acta Mater.* **61**, 2725 (2013).
- ³⁶ A. Vailionis, H. Boschker, W. Siemons, E. P. Houwman, D. H. A. Blank, G. Rijnders, and G. Koster, *Phys. Rev. B: Condens. Matter Mater. Phys.* **83**, 064101 (2011).
- ³⁷ F. Sandiumenge, J. Santiso, L. Balcells, Z. Konstantinovic, J. Roqueta, A. Pomar, J. Pedro Espinos, and B. Martinez, *Phys. Rev. Lett.* **110**, 107206 (2013).
- ³⁸ W. S. Choi, J. H. Kwon, H. Jeon, J. E. Hamann-Borrero, A. Radi, S. Macke, R. Sutarto, F. He, G. A. Sawatzky, V. Hinkov, M. Kim, and H. N. Lee, *Nano Lett.* **12**, 4966 (2012).
- ³⁹ L. J. van der Pauw, *Philips Res. Rep.* **13**, 1 (1958), available at: http://aki.issp.u-tokyo.ac.jp/okano/WalWiki/etc/VDP_PRR_13_1.pdf.
- ⁴⁰ N. F. Mott and E. A. Davis, *Electronic Processes in Non-Crystalline Materials* (Clarendon-Press, Oxford, 1971).
- ⁴¹ Y. Lu, J. Klein, F. Herbstritt, J. B. Philipp, A. Marx, and R. Gross, *Phys. Rev. B: Condens. Matter Mater. Phys.* **73**, 184406 (2006).